Light: Science & Applications (2017) 6, e17032; doi:10.1038/lsa.2017.32
Official journal of the CIOMP 2047-7538/17
www.nature.com/lsa

ORIGINAL ARTICLE

Three-dimensional super-resolution longitudinal magnetization spot arrays

Zhong-Quan Nie[1], Han Lin[2], Xiao-Fei Liu[3], Ai-Ping Zhai[1], Yan-Ting Tian[1], Wen-Jie Wang[1], Dong-Yu Li[4], Wei-Qiang Ding[5], Xue-Ru Zhang[5], Ying-Lin Song[5] and Bao-Hua Jia[1,2]

We demonstrate an all-optical strategy for realizing spherical three-dimensional (3D) super-resolution ($\sim\lambda^3/22$) spot arrays of pure longitudinal magnetization by exploiting a 4π optical microscopic setup with two high numerical aperture (NA) objective lenses, which focus and interfere two modulated vectorial beams. Multiple phase filters (MPFs) are designed via an analytical approach derived from the vectorial Debye diffraction theory to modulate the two circularly polarized beams. The system is tailored to constructively interfere the longitudinal magnetization components, while simultaneously destructively interfering the azimuthal ones. As a result, the magnetization field is not only purely longitudinal but also super-resolved in all three dimensions. Furthermore, the MPFs can be designed analytically to control the number and locations of the super-resolved magnetization spots to produce both uniform and nonuniform arrays in a 3D volume. Thus, an all-optical control of all the properties of light-induced magnetization spot arrays has been demonstrated for the first time. These results open up broad applications in magnetic-optical devices such as confocal and multifocal magnetic resonance microscopy, 3D ultrahigh-density magneto-optic memory, and light-induced magneto-lithography.
Light: Science & Applications (2017) **6,** e17032; doi:10.1038/lsa.2017.32; published online 25 August 2017

Keywords: inverse Faraday effect; longitudinal magnetization; magnetic-optical devices; magneto-optics; vectorial beams; vectorial Debye diffraction theory

INTRODUCTION

The interaction between light and magnetism is considered a promising route to the development of all-optical magnetic recording (AOMR)[1–3], confocal and magnetic resonance microscopy[4], atom trapping[5,6] and multi-dimensional magneto-optical data storage[7,8]. However, there are three key features demanded, which are also the key challenges in light-induced magnetization: (i) to achieve purely longitudinal magnetization (up to 100% in the focal region), allowing a well-defined magnetization direction in a material; (ii) to control the magnetization to an ultra-small 3D volume beyond the diffraction limit ($\sim\lambda^3/8$), which is essential for applications, including high-density magnetic-optical data storage and high-resolution magnetic resonance microscopy and (iii) to multiplex the magnetization spots into an array with a controllable spatial position for each spot, which will significantly enhance the processing speed and power efficiency of the opto-magnetic recording and reading, enabling the 3D manipulation of the trapped atoms. Therefore, there is a stringent demand to develop a highly efficient all-optical strategy that is able to produce 3D spherical longitudinal magnetization field arrays beyond the diffraction limit.

Numerous endeavors have been devoted to the development of ingenious polarization configurations[9,10] in conjunction with amplitude/phase modulation[11–13] that can simultaneously improve the longitudinal magnetization purity and compress the dimension of the light-induced magnetization field via the inverse Faraday effect[14–16]. To achieve a high spatial resolution for the light-induced magnetization, a high numerical aperture (NA) objective is required. However, the inherent depolarization effect along the axial direction[17] significantly degrades the purity of the longitudinal magnetization. Although a single spot of pure longitudinal magnetization can be achieved by using cylindrically polarized beams with a first-order vortex phase, a subwavelength spatial resolution can only be achieved along the lateral direction with a compromised resolution in the axial direction[10]. As a result, the overall magnetization volume is not improved. Moreover, although some strategies, for example, a superoscillatory lens, can achieve impressive resolution improvement, further development is required to eliminate the longitudinal polarization states in the focal region to achieve a pure longitudinal magnetization spot in the future[18,19]. Therefore, it is a great challenge to simultaneously realize high longitudinal magnetization purity and achieve 3D

[1]Key Lab of Advanced Transducers and Intelligent Control Systems, Ministry of Education of Shanxi Province, College of Physics and Optoelectronics, Taiyuan University of Technology, Taiyuan 030024, China; [2]Centre for Micro-Photonics, Faculty of Science, Engineering and Technology, Swinburne University of Technology, Hawthorn, Victoria 3122, Australia; [3]Department of Science, Taiyuan Institute of Technology, Taiyuan 030008, China; [4]Department of Physics, Lingnan Normal University, Zhanjiang 524048, China and [5]Department of Physics, Harbin Institute of Technology, Harbin 150001, China
Correspondence: BH Jia, Email: bjia@swin.edu.au
Received 14 September 2016; revised 14 February 2017; accepted 27 February 2017; accepted article preview online 1 March 2017

super-resolution along both the lateral and axial directions of the magnetization spot, which holds the key for most applications, in particular, for opto-magnetic data storage and lithography.

Here we propose and analytically demonstrate a 3D super-resolution ($\sim\lambda^3/22$) pure-longitudinal magnetization spot (MS) array with an individual spot size far below the diffraction limit ($\sim\lambda^3/8$) for the first time using a 4π high-NA focusing configuration[20–22]. Such a high resolution is achieved with ignorable side lobes ($<10\%$), which is generally challenging for any super-resolution technique[23,24], under the illumination of tailored circularly polarized Bessel–Gaussian (CPBG) beams[25]. By carefully manipulating the phase of the CPBG beams using multiple phase filters (MPFs), we can configure arbitrarily designed arrays of 3D super-resolution MSs with almost perfect uniformity (up to 100%) and symmetry (~97%). Our results provide the first viable solution to simultaneously and independently control all the properties of a magnetization spot array for developing the light-induced magnetic data storage and lithography devices.

MATERIALS AND METHODS

Opto-magnetization due to the inverse Faraday effect

To tackle the three fundamental challenges of light-induced magnetization, it is essential to understand its generation mechanism, originating from the inverse Faraday effect. For a magneto-optic (MO) material in Figure 1a, the conducting electrons can be regarded as a collisionless plasma, which can migrate freely[26]. The induced static magnetization in the MO material is the vector product of the electric field, which can be calculated as[14–16,27–29],

$$\mathbf{M}(r,\varphi,z) = i\gamma \mathbf{E}_t \times \mathbf{E}_t^{*} \tag{1}$$

where $\mathbf{E}_t^{*}$ denotes the complex conjugate of $\mathbf{E}_t$ and γ is the MO susceptibility. Therefore, the magnetizations of the magnets in the MO material in different directions are determined by the vectorial electric field components being polarized along different directions, as is schematically shown in Figure 1b. One can see that the longitudinal magnetization (M_z) is induced by the electric field components polarizing parallel to the focal plane (E_φ and E_r). Due to the strong electric field components along the optical axis (E_z) caused by the inherent depolarization effect of the high-NA objective, there exist significant transverse magnetization components (M_r and M_φ). Therefore, the key to achieving pure M_z is to eliminate the E_z component (Figure 1d) by destructive interference. Since the overall area of the magnetization spot is determined by the size of the focal spot of light (Figure 1a), reducing the size of the focal spot represents a viable approach to achieving 3D super-resolved magnetization spots (Figure 1c).

Optical scheme for achieving a pure-longitudinal MS

There are multiple ways to destructively interfere the E_z field component such as a phase singularity introduced by a vortex phase[30], a polarization singularity introduced by azimuthally polarized light[31,32] and a 4π microscopic system by counter-propagating two identically focused beams. Among those methods, the 4π microscopic system is preferred due to its capability in achieving the axial super-resolution simultaneously[20–22].

In a 4π microscopic system (Figure 2), the vectorial electric field distributions in the focal region can be calculated using the Debye diffraction theory (Supplementary Equations (1) and (2)). The interference of the focal fields of the two objectives is[33]

$$\mathbf{E}_t(r,\varphi,z) = \mathbf{E}_1(r,\varphi,z) + \mathbf{E}_2(-r,\varphi,-z) \tag{2}$$

where $\mathbf{E}_1$ and $\mathbf{E}_2$ stand for, respectively, the focal electric fields of the left and right objectives. The vectorial electric fields can be expressed as

$$\begin{aligned}\mathbf{E}_n = \mathbf{E}_{zn}(\pm r,\varphi,\pm z) + \mathbf{E}_{\varphi n}(\pm r,\varphi,\pm z)\\ + \mathbf{E}_{rn}(\pm r,\varphi,\pm z), n = 1,2\end{aligned} \tag{3}$$

where + is for the case $n=1$ and − is for the case $n=2$. The interference of the focal fields of the two objectives is

$$\mathbf{E}_{z,r,\varphi} = A_{z,r,\varphi}(r,\varphi,z)\ \exp\{i[\Phi_{z,r,\varphi}(r,\varphi) + \Phi_0 + kz]\} \tag{4}$$

A and Φ are the amplitude and phase distributions, respectively, and $k = 2\pi/\lambda$ is the wave vector of the incident light. The negative sign of r in $\mathbf{E}_2$ denotes the opposite orientations of the instantaneous polarizations of the two incident beams, which means $\Phi(r,\varphi)-\Phi(-r,\varphi)=\pi$,

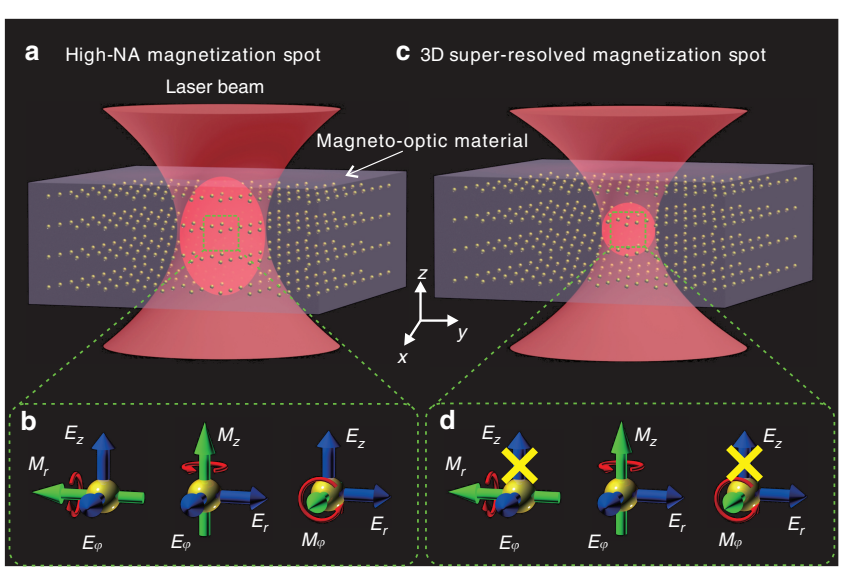

Figure 1 Comparison of the magnetization spot produced by a single high-NA objective (**a**) and a 3D pure longitudinal super-resolved magnetization spot (**c**). (**b**) Schematics of the magnetization mechanism due to the inverse Faraday effect in the focal region of a high-NA objective and (**d**) in the focal region of a 3D super-resolved focal spot. The crosses indicate the elimination of the E_z field component, leading to pure longitudinal magnetization.

doi:10.1038/lsa.2017.32

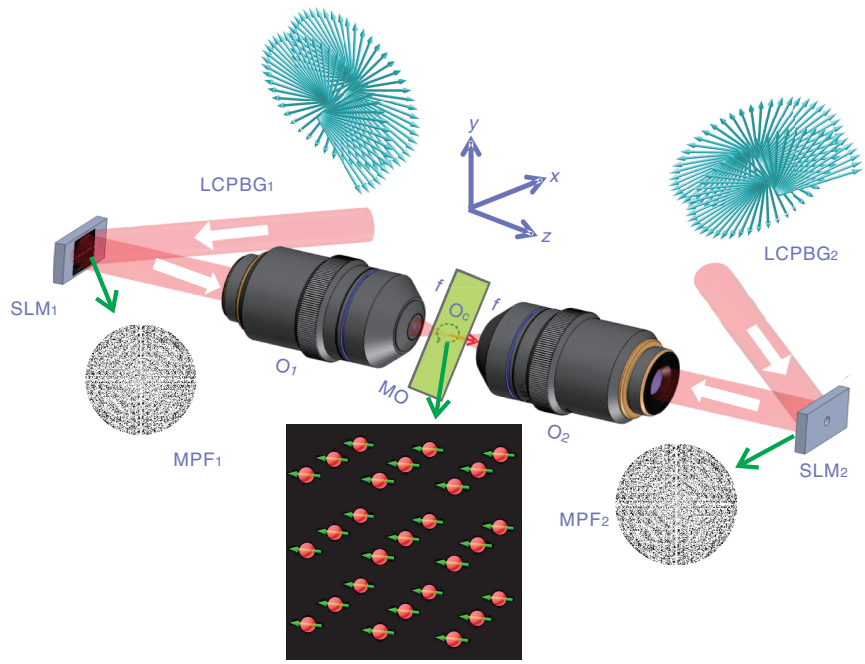

Figure 2 Schematics of a 4π high-NA objective lens-focusing configuration integrated with MPFs encoded by phase-only SLMs under the illumination of two counter-propagating CPBG beams. An MO medium locates at the confocal plane (O_c) of the proposed system. Bottom illustration: a 3× 3 ×3 3D super-resolution pure-longitudinal MS array. O_1, O_2: objective lenses. LCPBG: left-hand circularly polarized Bessel Gaussian.

whereas the negative sign of z in $\mathbf{E}_2$ indicates their counter-propagation nature, which means that the kz terms cancel each other. Φ_0 is the phase offset applied to the incident beams, and the phase difference between the two focal electric fields is $\Delta\Phi = \Phi_{01} - \Phi_{02}$.

From Equations (2)–(4), one can see that it is possible to constructively or destructively interfere the electric field components from the two objectives to enhance or suppress a particular field component by manipulating the amplitude A and the phase difference $\Delta\Phi$, which is determined by the polarization and phase of the incident beams. The E_z component can be completely removed if $A_{z1} = A_{z2}$ and $\Delta\Phi = 0$. On the other hand, it can be enhanced if $\Delta\Phi = \pi$ for incident light with any polarization state.

The previous strategy to achieve a pure longitudinal MS is to interfere two radially polarized vortex beams in the focal region of high-NA objective lenses in a 4π setup[34]. However, this strategy suffers from strong side lobes of up to 50% as strong as the intensity of the central peak due to the constructive interference of the longitudinal electric field components, rendering this method less attractive for practical applications[35]. Additionally, only a single magnetization spot was achieved previously, significantly limiting the processing efficiency. In addition, to be able to achieve a strong central focal spot in the transverse focal plane, a vortex phase ($\Phi(r,\varphi) = \varphi$) is required in cylindrically polarized light beams[10], which inevitably degrades their lateral resolutions. In comparison, circularly polarized beams have the advantage of a dominant transverse electric field in the center of the focal region to induce longitudinal magnetization. Therefore, circularly polarized incident beams have been selected in this study.

The conceptual design of the 4π microscopic system based setup is shown in Figure 2, where the incident beams are two counter-propagating CPBG beams with the same handedness of polarization, which illuminate on the spatial light modulators (SLMs)[36,37] and are focused by the high-NA objective lenses (NA = 1). Without additional phase modulation from the SLMs ($A_{z1} = A_{z2}$, and $\Delta\Phi = 0$), only M_z shows a non-zero value in the center of the focal region due to the removal of E_z. In addition, the transverse electric field components (E_r and E_φ) constructively interfere in the vicinity of the focus along both the z and r axes, which is favorable to sharpening the MS. Therefore, a single 3D super-resolution pure-longitudinal MS can be created by the two CPBG beams in the focal region. By modulating the wavefronts of the CPBG beams with the designed MPFs encoded by the SLMs, which consist of the superposition of the desired multiple off-focus and off-axis phase patterns, arrays of identical 3D super-resolution pure-longitudinal MSs can be created in an isotropic MO medium placed in the focal region perpendicular to the optical axis.

RESULTS AND DISCUSSION

Generation of 3D super-resolution MS via amplitude modulation

The shape of the focal spot can be controlled by varying the effective NA of the focusing objective through adjusting the amplitude distribution of the incident beam. Here we design the amplitude of the incident beam based on the Bessel–Gaussian (BG) function[25], which can be tuned by manipulating the order of the Bessel function (m) as

$$l_0(\theta) = \exp\left[-\left(\frac{\sin\theta}{\sin\alpha}\right)^2\right] J_m\left(\frac{2\sin\theta}{\sin\alpha}\right) \tag{5}$$

where l_0 is the amplitude distribution at the back aperture and θ and α are the convergence angle and the maximum, respectively. J_m is the mth Bessel function of the first kind. When $m = 0$, it is a Gaussian beam (Figure 3a). When m is a non-zero integer, a doughnut beam with a zero amplitude in the center is formed (Figure 3b and 3c). By increasing the value of m, the radius of the central zero amplitude is increased, which results in a higher effective NA, so that only the

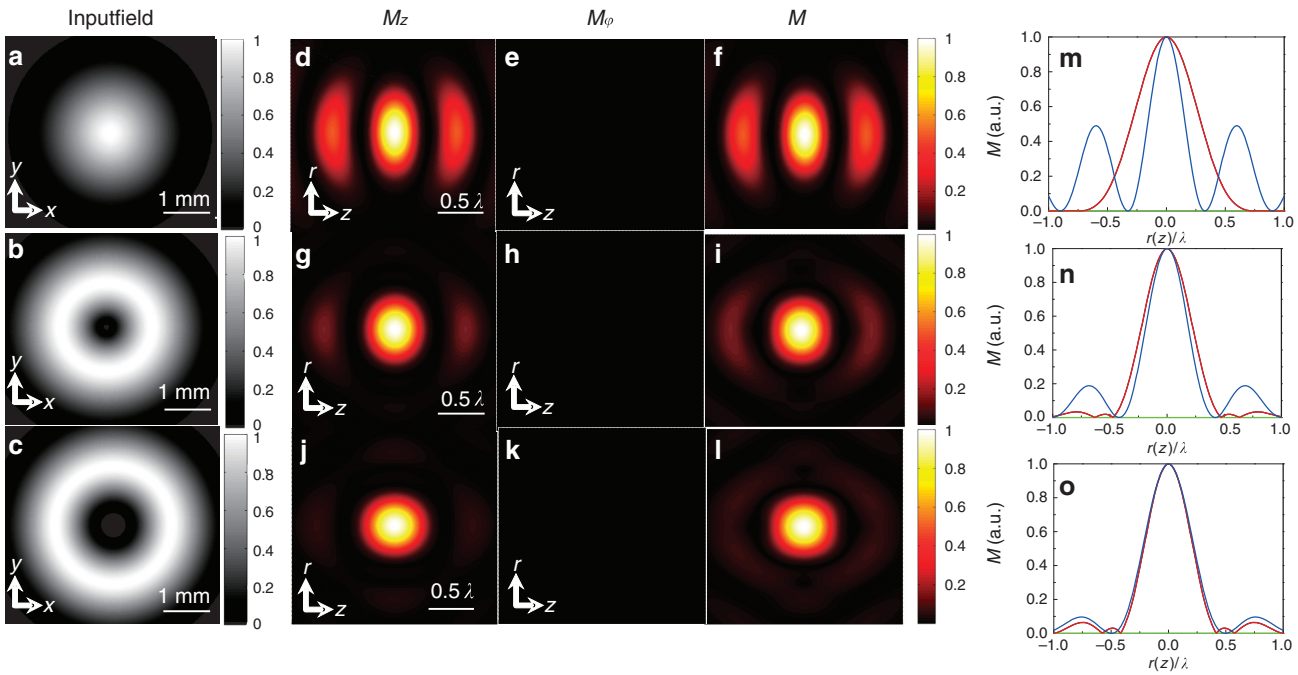

Figure 3 Column 1 (**a**–**c**): incident intensity distributions of the BG beams in the *xy* plane. (**d**–**l**) Light-induced magnetization distributions of tightly focusing CPBG beams with different *m* orders. (**d**–**f**) $m=0$, (**g**–**i**) $m=1$, (**j**–**l**) $m=2$. Column 2 (**d**, **g** and **j**) distributions of the longitudinal component M_z, column 3 (**c**, **h** and **k**) the azimuthal component M_φ, and column 4 (**f**, **i** and **l**) the total magnetization *M* in the *rz* plane. The dimension of the *xy* plane is 4×4 mm, and that of the *rz* plane is $2\lambda\times2\lambda$. Column 4 (**m**–**o**) represents the cross-sectional plots of the magnetization distributions for various orders. (**m**) $m=0$, (**n**) $m=1$, (**o**) $m=2$. The black, red and green curves denote *M*, M_φ and M_z along the *r* axis, and the blue curve represents M along the *z* axis.

components with a large convergence angle are focused by the objectives. Therefore, two effects are evident in the focal region: (i) the lateral resolution of the MS becomes higher and (ii) the axial resolution of the MS becomes lower. In this way, by properly searching for the balance point, it is possible to achieve the MS with the best resolution along all the three directions. In addition, due to the focal spot elongation in the axial direction, the side lobe of the MS is minimized.

The resulting magnetization distributions of BG beams of different orders ($m=0$, 1 and 2) are shown in Figure 3. Since the nonzero radial magnetization component (M_r) only appears in the out-of-focus region, it is not shown here. Compared to the case of one CPBG beam focused by a single high-NA objective (Supplementary Figs. S1 and S2), the azimuthal magnetization component (M_φ) vanishes completely regardless of the beam order (Figure 3e, 3h and 3k), leading to pure longitudinal magnetization (Figure 2f, 2i and 2l). In addition, the full width at half maximum (FWHM) values along the axial direction are enormously suppressed by the 4π system (Figure 3m), and the FWHM in the axial direction (W_z), which in the transverse direction (W_r) and the strength of the side lobes are tunable by the order of the Bessel function (Figure 3n and 3o). It is found that a remarkable almost spherical (aspect ratio of 97%) and 3D super-resolution MS can be achieved at the optimized position when $m=2$ (Figure 3o). In the meantime, the maximal side lobe strength is only 9.6% of the central peak along the axial direction (black line in Figure 3o). Such exceptionally low side lobes significantly distinguish the current approach from that of the 4π strongly focused cylindrically polarized vortex beams with previously reported side lobes of $>50\%$[34]. The calculated W_r are 0.592λ, 0.470λ and 0.435λ for $m=0$, 1 and 2 (Figure 3m–3o), respectively, while the W_z are 0.319λ, 0.395λ and 0.449λ, respectively, which are significantly smaller than the wavelength. It is obvious that W_r and W_z follow an opposite trend as predicted. To further verify these trends, we select the higher beam order of $m=4$ to portray the light-induced magnetization pattern (Supplementary Fig. S3). It is obvious that the value of W_z has increased, leading to a much larger MS compared to the optimized case at $m=2$.

The overall magnetization distribution of the spot is plotted in Figure 4a, which shows pure longitudinal magnetization in the focal region. In comparison, the single-objective case shows a strong azimuthal magnetization in the focal region (Figure 4b), resulting in a 3D polarized magnetization (marked by the two green ellipses) due to the existence of the E_z light field component. To further show the magnetization profile, corresponding 3D iso-surface plots of the magnetization are shown in Figure 4c and 4d, where the 3D super-resolved quasi-spherical magnetization field can be clearly identified. To evaluate the best achievable 3D magnetization resolution, the voxel size of the MS can be calculated as $4\pi/3\times(W_r/2)^2\times W_z/2$, where the MS is approximated as an ellipsoid. In the optimized case of $m=2$, a 3D minimum MS with a super-resolved voxel of $\sim\lambda^3/22$ (Figure 4c) can be achieved, far smaller than the diffraction limit of $\lambda^3/8$. This 3D super-resolved quasi-spherical MS can find enormous potential applications in ultra-compact opto-magnetic devices[38,39] and confocal and magnetic resonance microscopy[4]. For example, based on the best-achieved 3D resolution, the storage density in the MO material is estimated to be 45 Tbits cm^{-3}, which is 2.2 Tbits inch^{-2} (at an 800-nm illumination wavelength) in terms of areal density,

doi:10.1038/lsa.2017.32

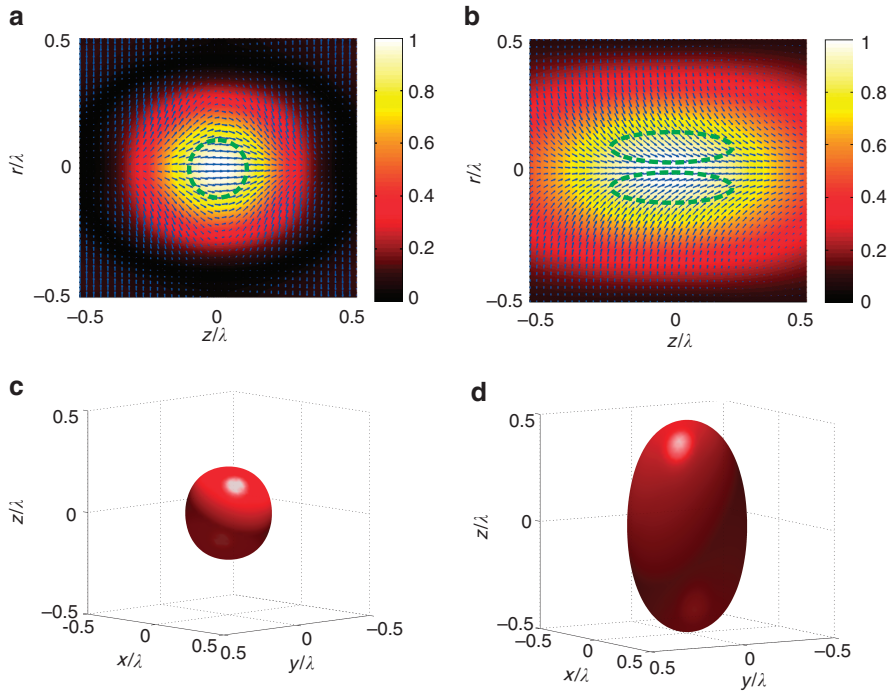

Figure 4 Comparisons of the polarization patterns and the 3D light-induced iso-magnetization surfaces for the case of $m=2$. Top: polarization distributions of the 4π focusing system (**a**) and the single-objective focusing system (**b**). Bottom: 3D iso-magnetization surfaces located at 50% of the maximum magnetization of the 4π focusing system (**c**) and the single-objective focusing system (**d**).

outperforming the state-of-the-art hard drive disk based on sophisticated nanofabrication technology.

Creation of 3D super-resolution longitudinal magnetization arrays via MPF

For real-life applications, improving the processing efficiency by using the 3D super-resolution longitudinal MSs requires creating MS arrays with arbitrarily controlled spot locations and numbers. The current approach to generate a multifocal array is to iteratively optimize the phase modulation at the back aperture of the objective to achieve the desired intensity distribution of arrays in the focal region[40,41]. This iterative approach is not only time-consuming but also lacks physical insight. Therefore, here we propose and demonstrate an analytical method to generate the desired MS arrays by using MPFs (Figure 5a). To calculate the phase distribution at the back aperture analytically, we convert the vectorial diffraction integral (Supplementary Equation (1)) into a Fourier transform of the weighted field (Supplementary Equation (8)). In this way, the electric field distribution in the focal region is the convolution of the Fourier transform of the phase modulation provided by the MPFs and the Fourier transform of the incident electric field of a CPBG beam with a plane wavefront (Supplementary Section 2). Therefore, the phase function of the MPFs can be calculated analytically as

$$t(x,y)=\sum_{g=1}^{G}\sum_{s=1}^{S}\exp\left[-i2\pi\left(\pm a_g x\pm y b_s\right)\right]\times\sum_{t=1}^{T}\exp\left(\pm ikc_t\cos\theta\right) \tag{6}$$

where G, S, and T are integers, giving the entire numbers of spots along the x, y and z directions, respectively; g, s and t, in sequence, ranging from 1 to G, 1 to S and 1 to T; and (a_g, b_s) and c_t represent the lateral and axial displacements, respectively. Therefore, the phase function is a superposition of the electric fields of each spot at the back aperture.

Here we take the MPFs with an equidistant interval of $a_g=b_s=c_t=8\lambda$ and fixed unit number of $G=S=T=4$ as an example. The resulting phase pattern (Figure 5a) arranges periodically in the entire pupil plane to shift the single MS to the appointed positions along both the transverse and axial directions. This behaves as a distinct and versatile phase-only 3D grating[42,43]. Figure 5b represents the 3D iso-magnetization surface of the induced magnetization distribution at $M=M_{\max}/2$ when the optimized phase pattern (Figure 5a) is imposed on the incoming beams at the pupil plane. It is shown that a $4\times4\times4$ MS array can be produced, and the spacing between adjacent layers is 8λ. Cross-section maps of the 3D MS array in the xy and rz planes are shown in Figure 5c and 5d, respectively. More importantly, the 3D resolution of any MS (white dashed lines in Figure 5c and 5d) is identical to the case without modulation from the MPFs (Figure 5e). Furthermore, the magnetization direction of each spot inside the array is completely longitudinal within the main lobe, which is identical to the case for the single MS (Figure 5f). The same principle can be used to create multifocal spot arrays with an arbitrary number of spots and configuration, which is analogous to the corresponding optical arrays[44–47]. The cases of $2\times2\times2$ and $3\times3\times3$ MS arrays are demonstrated in Supplementary Figs. S4 and S5. Here we compare the absolute values of a single magnetization spot and a magnetization spot in an array. The energy conversion efficiency is also studied by summing up the overall energy in the array and comparing the value to that of a single spot. It has been found that more than 90% of the overall energy distributes uniformly to the spots in the array.

In addition to the spatial resolution and polarization, two other important parameters are defined to evaluate the performance of the MS arrays: (i) the uniformity of the magnetization amplitude, which is defined as $1-D$, where D represents the maximum difference among

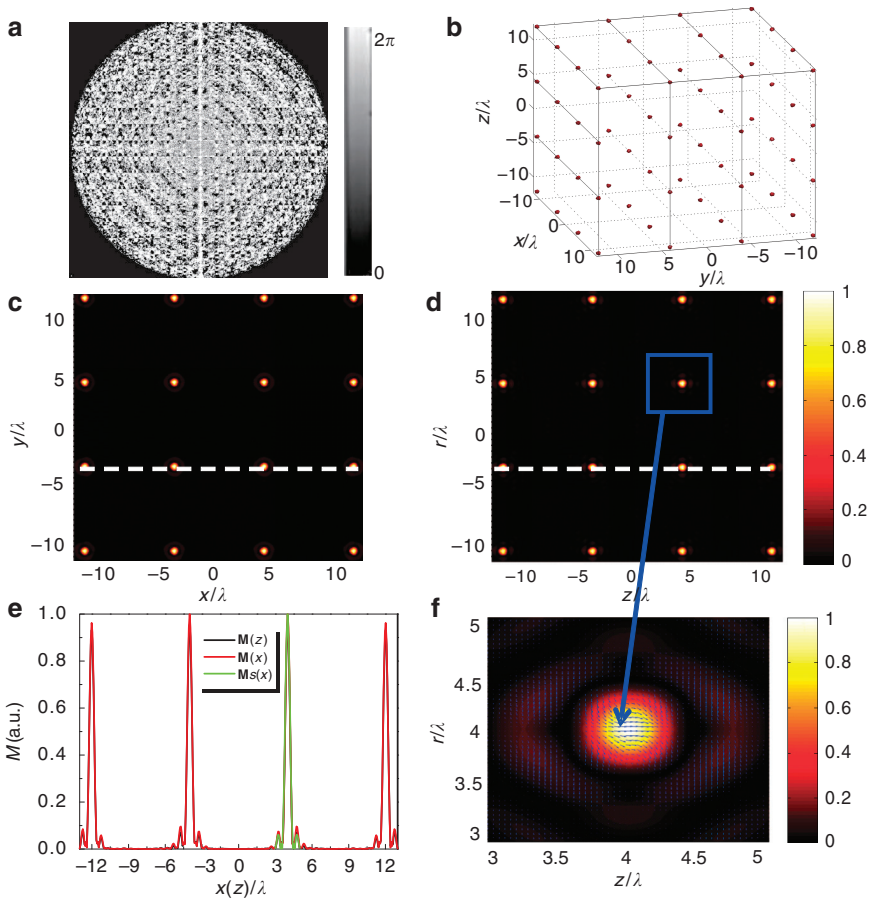

Figure 5 The $4\times4\times4$ 3D super-resolution longitudinal MS array induced by the optimized MPFs acting on the left-handed circularly polarized BG beams in the 4π focusing geometry. (**a**) Phase pattern of the MPFs with $G=S=T=4$ and $a_g=b_s=c_t=8\lambda$. (**b**) 3D iso-magnetization surface of the MS array with $M=M_{max}/2$. (**c** and **d**) Contour plots of the total magnetization field in the *xy* and *rz* planes. (**e**) Relevant magnetization cross-section profiles in **c** and **d**, respectively (black and red lines are along the *x* and *z* axes, respectively. The green line represents the *x* axis cross-section of the magnetization pattern of a single focal spot without the use of MPFs. (**f**) Enlarged individual spot inside the MS array and its polarization distribution in the *rz* plane.

all MSs in the normalized magnetization distribution and (ii) a spherically symmetrical distribution for each MS[48]. The optimized uniformities are 100%, 98.4% and 96.4% for two-layer, three-layer and four-layer 3D super-resolution longitudinal MS arrays, respectively (Figure 5e, also see Supplementary Figs. S4e and S5e). Such a high uniformity can offer an excellent tolerance in multilayer magnetic-optical recording and maintain high accuracy in multifocal magnetic resonance imaging. The aspect ratio of all spots is ~97% for any 3D super-resolution longitudinal MS array. It is important to note that there are two fundamental differences compared with the light-triggered magnetization chain[49]. First, the MS array reported here is highly uniform, while the induced magnetization chain gradually weakens from the geometric focus. Additionally, each MS in the array is 3D super-resolved, whereas the counterpart in the chain is only transversely super-resolved.

Aperiodic and asymmetric multilayer MS arrays can also be induced by designing more tailored MPFs. Here we take an Archimedean spiral 3D super-resolution longitudinal MS array as an example. To this end, the phase function of the MPFs in Equation (4) should be replaced by the formula:

$$t(x,y)=\sum_{g=1}^{G}\exp\left[-i2\pi\left(a_g x+b_g y\right)\right]\exp\left(ikc_g\cos\theta\right) \qquad (7)$$

with $a_g=t_g\cos(t_g)$, $b_g=t_g\sin(t_g)$, $t_g\in(0,\ 2\pi)\times g/G$, $c_g=(0,\ 4\pi)\times g/G$, and G represents the total number of MSs in the curved array. Under such a circumstance, Figure 6 depicts the Archimedean spiral 3D super-resolution longitudinal MS array with $G=18$. It is observed from Figure 6a that the phase diagram of the renewed MPF presents a spiral and helical pattern. Figure 6b shows the 3D iso-magnetization surface ($M=M_{max}/2$) of the MS array when the incident fields are modulated by the spiral phase revealed in Figure 6a. As expected, an MS array is created with 18 spots in an Archimedean spiral pattern, where each spot locates at its predetermined spatial position in a robust way. To visualize the demonstrated magnetization feature more intuitively, we produce cross-section maps of the 3D Archimedean spiral-shaped MS array in the *xy* and *rz* planes, respectively, as shown in Figure 6c and 6d. Further, it is revealed that the resolution of any MS (the blue rectangle regime in Figure 6f) is almost the same as the value without being subjected to the spiral MPFs (Figure 6e). We also find that the magnetization direction of the selected MS inside the array is purely longitudinal (Figure 6f). It should be noted that the aspect ratio of the MS in the Archimedean spiral array is ~97%, and the relevant uniformity is 90% (Figure 6c and 6d).

From the experimental perspective, multiple phase filters can be encoded by a dynamic and phase-only spatial light modulator (SLM)

doi:10.1038/lsa.2017.32

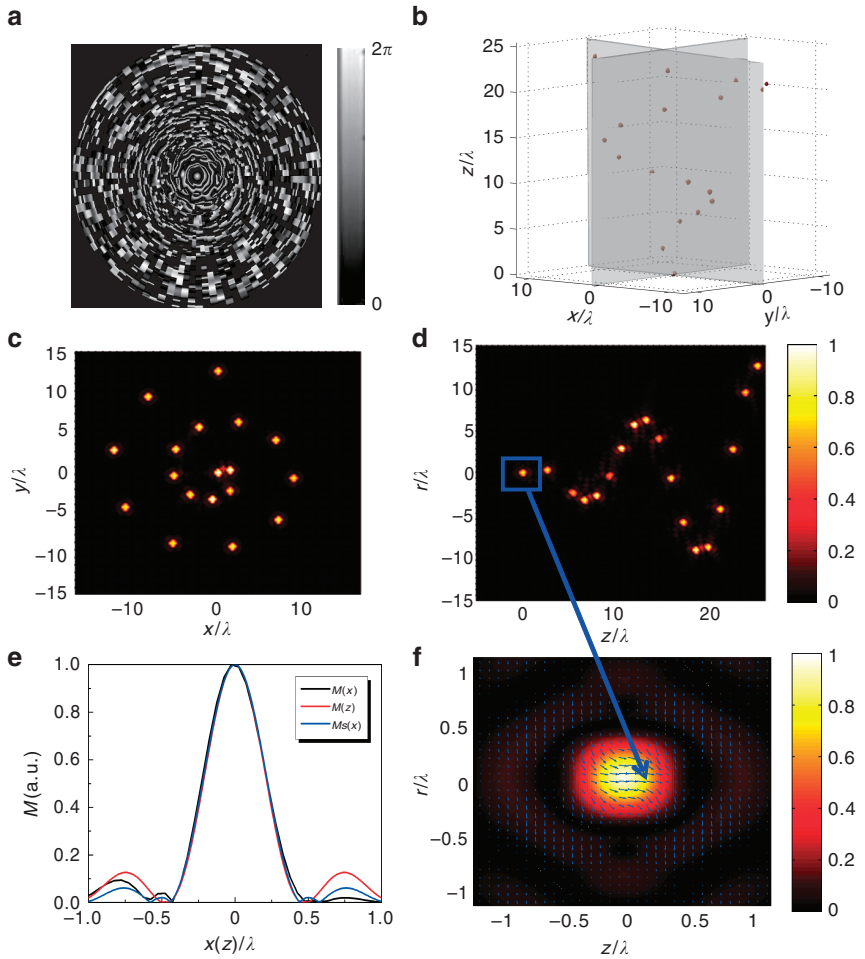

Figure 6 Archimedean spiral 3D super-resolution longitudinal MS array. (**a**) Phase pattern of the MPFs with $G=18$. (**b**) 3D iso-magnetization surface of the MS array with $M=M_{max}/2$. (**c** and **d**) Perspective views of the total magnetization field in the *xy* and *rz* planes. (**e**) Relevant magnetization cross-section profiles in **c** and **d**, respectively (black and red lines are the magnetization cross-section profiles in the array along the *x* and *z* axes, respectively. The blue line represents the magnetization pattern of a single focal spot without the MPFs along the *x* axis). (**f**) Enlarged view of individual MS inside the array and its polarization distribution in the *rz* plane.

to realize three-dimensional super-resolution longitudinal magnetization spot arrays. The current commercially available SLMs (for example, Holoeye Pluto) are able to produce 256 levels of phase modulation in the range of 0–2π. The errors in the phase modulation can be minimized by phase calibration to tune the gamma curve. In this way, we expect less than 5% error in the phase modulation. It should be noted that the phase-only SLM must have at least 8 modulation levels to achieve a highly uniform (90%) spot array[36,37]. To consider the effect of errors in the phase modulation, we implement 10% randomness in the phase modulation in our simulation, resulting in only minor decreases (~3%) in the efficiency and uniformity of the array.

CONCLUSIONS

In summary, we have theoretically demonstrated light-induced magnetization by tightly focusing two modulated circularly polarized BG beams in the 4π configuration. Due to the destructive interference of the axial electric field component, a pure longitudinal MS is achieved. Through amplitude modulation based on the BG function, a quasi-spherical 3D super-resolution ($\sim\lambda^3/22$) MS with ignorable side lobes has been demonstrated for the first time. More significantly, arbitrary MS arrays, for example, Archimedean spiral 3D super-resolution longitudinal MS arrays, can be generated by MPFs, designed analytically according to the location and number of the MSs. The generated MS arrays exhibit excellent uniformity and almost spherical symmetry, making them an appealing platform for developing light-induced magneto-lithography devices. Most importantly, using the proposed method, all three properties of a MS array, namely, the magnetization direction, the 3D resolution and the number and arrangement of the MSs, can be simultaneously and independently controlled, which makes this method extremely flexible. One can arbitrarily adjust any of the properties depending on the application requirements without compromising the others. The demonstrated light-induced magnetization might also shed light on the spin–spin interaction, which ignites a new research field in magnonics[50]. From an experimental perspective, the possibility of achieving powerful MS arrays using circularly polarized beams with robust MPFs is particularly fascinating due to the application of dynamic SLMs[34,35]. The MS arrays can be applied broadly in multiple atom trapping and transport, confocal and multifocal magnetic resonance imaging, and multilayer magneto-optical recording and storage. The uniform longitudinal MS arrays can also be applied to light-induced magneto-lithography devices with high efficiency[51,52].

CONFLICT OF INTEREST

The authors declare no conflict of interest.

ACKNOWLEDGEMENTS

This work was supported by the National Natural Science Foundation of China (Nos. 61575139, 11474077, 11374079, 11604236, 51602213, 61605136 and 11404283), Fundamental & advanced research projects of Chongqing, China (cstc2013jcyjC00001), the Youth Foundation of the Taiyuan University of Technology (No. 2015QN066), the Youth Science Foundation of the Taiyuan Institute of Technology (No. 2015LQ14), the Science and Technology Program of Guangdong (2016A040403124) and the Shanxi Scholarship Council of China (No. 2013-037).

1 Stanciu CD, Hansteen F, Kimel AV, Kirilyuk A, Tsukamoto A *et al*. All-optical magnetic recording with circularly polarized light. *Phys Rev Lett* 2007; **99**: 047601.
2 Khorsand AR, Savoini M, Kirilyuk A, Kimel AV, Tsukamoto A *et al*. Role of magnetic circular dichroism in all-optical magnetic recording. *Phys Rev Lett* 2012; **108**: 127205.
3 Mangin S, Gottwald M, Lambert CH, Steil D, Uhlíř V *et al*. Engineered materials for all-optical helicity-dependent magnetic switching. *Nat Mater* 2014; **13**: 286–292.
4 Grinolds MS, Warner M, de Greve K, Dovzhenko Y, Thiel L *et al*. Subnanometre resolution in three-dimensional magnetic resonance imaging of individual dark spins. *Nat Nanotechnol* 2014; **9**: 279–284.
5 Vetsch E, Reitz D, Sagué G, Schmidt R, Dawkins ST *et al*. Optical interface created by laser-cooled atoms trapped in the evanescent field surrounding an optical nanofiber. *Phys Rev Lett* 2010; **104**: 203603.
6 Schneeweiss P, Le Kien F, Rauschenbeutel A. Nanofiber-based atom trap created by combining fictitious and real magnetic fields. *New J Phys* 2014; **16**: 013014.
7 Zijlstra P, Chon JWM, Gu M. Five-dimensional optical recording mediated by surface plasmons in gold nanorods. *Nature* 2009; **459**: 410–413.
8 Gu M, Li XP, Gao YY. Optical storage arrays: a perspective for future big data storage. *Light Sci Appl* 2014; **3**: e177, doi:10.1038/lsa.2014.58.
9 Wang SC, Li XP, Zhou JY, Gu M. All-optically configuring the inverse Faraday effect for nanoscale perpendicular magnetic recording. *Opt Express* 2015; **23**: 13530–13536.
10 Jiang YS, Li XP, Gu M. Generation of sub-diffraction-limited pure longitudinal magnetization by the inverse Faraday effect by tightly focusing an azimuthally polarized vortex beam. *Opt Lett* 2013; **38**: 2957–2960.
11 Ravi V, Suresh P, Rajesh KB, Jaroszewicz Z, Anbarasan PM *et al*. Generation of sub-wavelength longitudinal magnetic probe using high numerical aperture lens axicon and binary phase plate. *J Opt* 2012; **14**: 055704.
12 Wang SC, Li XP, Zhou JY, Gu M. Ultralong pure longitudinal magnetization needle induced by annular vortex binary optics. *Opt Lett* 2014; **39**: 5022–5025.
13 Ma WZ, Zhang DW, Zhu LW, Chen JN. Super-long longitudinal magnetization needle generated by focusing an azimuthally polarized and phase-modulated beam. *Chin Opt Lett* 2015; **13**: 052101.
14 Pitaevskiĭ LP. Electric forces in a transparent dispersive medium. *Sov Phys JETP* 1961; **12**: 1008–1013.
15 van der Ziel JP, Pershan PS, Malmstrom LD. Optically-induced magnetization resulting from the inverse Faraday effect. *Phys Rev Lett* 1965; **15**: 190–193.
16 Kimel AV, Kirilyuk A, Rasing T. Femtosecond opto-magnetism: ultrafast laser manipulation of magnetic materials. *Laser Photonics Rev* 2007; **1**: 275–287.
17 Jia BH, Gan XS, Gu M. Direct measurement of a radially polarized focused evanescent field facilitated by a single LCD. *Opt Express* 2005; **13**: 6821–6827.
18 Ye HP, Qiu CW, Huang K, Teng JH, Luk'yanchuk B *et al*. Creation of a longitudinally polarized subwavelength hotspot with an ultra-thin planar lens: vectorial Rayleigh-Sommerfeld method. *Laser Phys Lett* 2013; **10**: 065004.
19 Huang K, Ye HP, Teng JH, Yeo SP, Luk'yanchuk B *et al*. Optimization-free super-oscillatory lens using phase and amplitude masks. *Laser Photonics Rev* 2014; **8**: 152–157.
20 Bokor N, Davidson N. Toward a spherical spot distribution with 4π focusing of radially polarized light. *Opt Lett* 2004; **29**: 1968–1970.
21 Chen WB, Zhan QW. Creating a spherical focal spot with spatially modulated radial polarization in 4Pi microscopy. *Opt Lett* 2009; **34**: 2444–2446.
22 Yu YZ, Zhan QW. Creation of identical multiple focal spots with prescribed axial distribution. *Sci Rep* 2015; **5**: 14673.
23 Urbach HP, Pereira SF. Field in focus with a maximum longitudinal electric component. *Phys Rev Lett* 2008; **100**: 123904.
24 Mudry E, Le Moal E, Ferrand P, Chaumet PC, Sentenac A. Isotropic diffraction-limited focusing using a single objective lens. *Phys Rev Lett* 2010; **105**: 203903.
25 Gu M. *Advanced Optical Imaging Theory*. Berlin Heidelberg: Springer; 2000.
26 Hertel R. Theory of the inverse Faraday effect in metals. *J Magn Magn Mater* 2006; **303**: L1–L4.
27 Taguchi K, Ohe JI, Tatara G. Ultrafast magnetic vortex core switching driven by the topological inverse Faraday effect. *Phys Rev Lett* 2010; **109**: 127204.
28 Kimel AV, Kirilyuk A, Usachev PA, Pisarev RV, Balbashov AM *et al*. Ultrafast non-thermal control of magnetization by instantaneous photomagnetic pulses. *Nature* 2005; **435**: 655–657.
29 Kirilyuk A, Kimel AV, Rasing T. Ultrafast optical manipulation of magnetic order. *Rev Mod Phys* 2010; **82**: 2731–2784.
30 Sheppard CJR. Polarized focused vortex beams: half-order phase vortices. *Opt Express* 2014; **22**: 18128–18141.
31 Yuan GH, Wei SB, Yuan XC. Nondiffracting transversally polarized beam. *Opt Lett* 2011; **36**: 3479–3481.
32 Qin F, Huang K, Wu JF, Jiao J, Luo XG *et al*. Shaping a subwavelength needle with ultra-long focal length by focusing azimuthally polarized light. *Sci Rep* 2015; **5**: 9977.
33 Chen GY, Song F, Wang HT. Sharper focal spot generated by 4π tight focusing of higher-order Laguerre-Gaussian radially polarized beam. *Opt Lett* 2013; **38**: 3937–3940.
34 Nie ZQ, Ding WQ, Li DY, Zhang XR, Wang YX *et al*. Spherical and sub-wavelength longitudinal magnetization generated by 4π tightly focusing radially polarized vortex beams. *Opt Express* 2015; **23**: 690–701.
35 Li Q, Zhao X, Zhang B, Zheng Y, Zhou LQ *et al*. Nanofocusing of longitudinally polarized light using absorbance modulation. *Appl Phys Lett* 2014; **104**: 061103.
36 Wang XL, Chen J, Li YN, Ding JQ, Guo CS *et al*. Optical orbital angular momentum from the curl of polarization. *Phys Rev Lett* 2010; **105**: 253602.
37 Shrestha PK, Chun YT, Chu DP. A high-resolution optically addressed spatial light modulator based on ZnO nanoparticles. *Light Sci Appl* 2015; **4**: e259, doi:10.1038/lsa.2015.32.
38 Lambert CH, Mangin S, Varaprasad BSDChS, Takahashi YK, Hehn M *et al*. All-optical control of ferromagnetic thin films and nanostructures. *Science* 2014; **345**: 1337–1340.
39 Li XP, Cao YY, Tian N, Fu L, Gu M. Multifocal optical nanoscopy for big data recording at 30 TB capacity and gigabits/second data rate. *Optica* 2015; **2**: 567–570.
40 Ren HR, Lin H, Li XP, Gu M. Three-dimensional parallel recording with a Debye diffraction-limited and aberration-free volumetric multifocal array. *Opt Lett* 2014; **39**: 1621–1624.
41 Mu TK, Chen ZY, Pacheco S, Wu RM, Zhang CM *et al*. Generation of a controllable multifocal array from a modulated azimuthally polarized beam. *Opt Lett* 2016; **41**: 261–264.
42 Zhang B, Wang ZR, Brodbeck S, Schneider C, Kamp M *et al*. Zero-dimensional polariton laser in a subwavelength grating-based vertical microcavity. *Light Sci Appl* 2014; **3**: e135, doi:10.1038/lsa.2014.16.
43 Lee HC, Na JY, Moon YJ, Park JS, Ee HS *et al*. Three-dimensional grating nanowires for enhanced light trapping. *Opt Lett* 2016; **41**: 1578–1581.
44 Lin H, Jia BH, Gu M. Dynamic generation of Debye diffraction-limited multifocal arrays for direct laser printing nanofabrication. *Opt Lett* 2011; **36**: 406–408.
45 Gu M, Lin H, Li XP. Parallel multiphoton microscopy with cylindrically polarized multifocal arrays. *Opt Lett* 2013; **38**: 3627–3630.
46 Lin H, Gu M. Creation of diffraction-limited non-Airy multifocal arrays using a spatially shifted vortex beam. *Appl Phys Lett* 2013; **102**: 084103.
47 Zhu LW, Sun MY, Zhang DW, Yu JJ, Wen J *et al*. Multifocal array with controllable polarization in each focal spot. *Opt Express* 2015; **23**: 24688–24698.
48 Guo HM, Dong XM, Weng XY, Sui GR, Yang N *et al*. Multifocus with small size, uniform intensity, and nearly circular symmetry. *Opt Lett* 2011; **36**: 2200–2202.
49 Nie ZQ, Ding WQ, Shi G, Li DY, Zhang XR *et al*. Achievement and steering of light-induced sub-wavelength longitudinal magnetization chain. *Opt Express* 2015; **23**: 21296–21305.
50 Neusser S, Grundler D. Magnonics: spin waves on the nanoscale. *Adv Mater* 2009; **21**: 2927–2932.
51 Feng L, Romulus J, Li MF, Sha RJ, Royer J *et al*. Cinnamate-based DNA photolithography. *Nat Mater* 2013; **12**: 747–753.
52 Shi R, Huang CZ, Zhang LF, Amini A, Liu K *et al*. Three dimensional sculpturing of vertical nanowire arrays by conventional photolithography. *Sci Rep* 2016; **6**: 18886.

This work is licensed under a Creative Commons Attribution-NonCommercial-ShareAlike 4.0 International License. The images or other third party material in this article are included in the article's Creative Commons license, unless indicated otherwise in the credit line; if the material is not included under the Creative Commons license, users will need to obtain permission from the license holder to reproduce the material. To view a copy of this license, visit http://creativecommons.org/licenses/by-nc-sa/4.0/

© The Author(s) 2017

Supplementary Information for this article can be found on the *Light: Science & Applications*' website (http://www.nature.com/lsa).